YALE PEABODY MUSEUM

JOURNAL OF MARINE RESEARCH

The *Journal of Marine Research,* one of the oldest journals in American marine science, published important peer-reviewed original research on a broad array of topics in physical, biological, and chemical oceanography vital to the academic oceanographic community in the long and rich tradition of the Sears Foundation for Marine Research at Yale University.

An archive of all issues from 1937 to 2021 (Volume 1–79) are available through EliScholar, a digital platform for scholarly publishing provided by Yale University Library at https://elischolar.library.yale.edu/.

Requests for permission to clear rights for use of this content should be directed to the authors, their estates, or other representatives. The *Journal of Marine Research* has no contact information beyond the affiliations listed in the published articles. We ask that you provide attribution to the *Journal of Marine Research.*

Yale University provides access to these materials for educational and research purposes only. Copyright or other proprietary rights to content contained in this document may be held by individuals or entities other than, or in addition to, Yale University. You are solely responsible for determining the ownership of the copyright, and for obtaining permission for your intended use. Yale University makes no warranty that your distribution, reproduction, or other use of these materials will not infringe the rights of third parties.

Linear instabilities of a two-layer geostrophic surface front near a wall

by Angelique C. Haza[1,2], Nathan Paldor[1,3] and Arthur J. Mariano[1]

ABSTRACT

The development of linear instabilities on a geostrophic surface front in a two-layer primitive equation model on an *f*-plane is studied analytically and numerically using a highly accurate differential shooting method. The basic state is composed of an upper layer in which the mean flow has a constant potential vorticity, and a quiescent lower layer that outcrops between a vertical wall and the surface front (defined as the line of intersection between the interface that separates the two layers and the ocean's surface). The characteristics of the linear instabilities found in the present work confirm earlier results regarding the strong dependence of the growth rate (σ_i) on the depth ratio *r* (defined as the ratio between the total ocean depth and the upper layer's depth at infinity) for $r \geq 2$ and their weak dependence on the distance *L* between the surface front and the wall. These earlier results of the large *r* limit were obtained using a much coarser, algebraic, method and had a single maximum of the growth rate curve at some large wavenumber *k*. Our new results, in the narrow range of $1.005 \leq r \leq 1.05$, demonstrate that the growth rate curve displays a second lobe with a local (secondary) maximum at a nondimensional wavenumber (with the length scale given by the internal radius of deformation) of 1.05. A new "fitting function" $0.183 \ r^{-0.87}$ is found for the growth rate of the most unstable wave (σ_{imax}) for *r* ranging between 1.001 and 20, and for $L > 2R_d$ (i.e. where the effect of the wall becomes negligible). Therefore, σ_{imax} converges to a finite value for $|r - 1| \ll 1$ (infinitely thin lower layer). This result differs from quasi-geostrophic, analytic solutions that obtain for the no wall case since the QG approximation is not valid for very thin layers. In addition, an analytical solution is derived for the lower-layer solutions in the region between the wall and the surface front where the upper layer is not present. The weak dependence of the growth rate on *L* that emerges from the numerical solution of the eigenvalue problem is substantiated analytically by the way *L* appears in the boundary conditions at the surface front. Applications of these results for internal radii of deformation of 35–45 km show reasonable agreement with observed meander characteristics of the Gulf Stream downstream of Cape Hatteras. Wavelengths and phase speeds of (180–212 km, 39–51 km/day) in the vicinity of Cape Hatteras were also found to match with the predicted dispersion relationships for the depth-ratio range of $1^+ < r < 2$.

1. Division of Meteorology and Physical Oceanography, Rosenstiel School of Marine and Atmospheric Science, University of Miami, Miami, Florida 33149, U.S.A.
2. Corresponding author. *email: ahaza@rsmas.miami.edu*
3. Department of Atmospheric Sciences, Institute of Earth Sciences, Hebrew University of Jerusalem, Jerusalem 91904, Israel.

1. Introduction

Observations of Gulf Stream meanders (or time-dependent wavelike lateral displacements) have revealed a broad variability spectrum, the characteristics of which vary widely depending on the exact location and time of observation along the Stream. The dominant meanders south of Cape Hatteras have wavelengths of 100–250 km and downstream propagating phase speeds of 30–45 km/day, with weekly and 3–4 day periods (Brooks and Bane, 1981). Tracey and Watts (1986) find rapid growth rates near Cape Hatteras in two separate bands for periods and wavelengths of 4–5 days, 180–230 km and 10–33 days, 300–500 km, with downstream propagation phase speeds increasing from 14 to 45 km/day. Between 70W and 74W, Gulf Stream meanders exhibit rapid downstream growth, with a maximum corresponding to 3-day *e*-folding times for wavelengths and periods of 260 km and 8 days (Kontoyiannis and Watts, 1994), while large amplitude meanders east of 70W were observed with 200–400 km wavelengths and propagation speeds of 5–10 km/day (Halliwell and Mooers, 1983). At 68W, meanders tend to stall and form large amplitude troughs, resulting in the pinching off of eddies through a baroclinic conversion process (Cronin and Watts, 1996; Cronin, 1996).

Linear instability theory is commonly invoked to explain the observed growth of meander's amplitude in a geostrophic current. Following the pioneering work of Orlanski (1968), analytical and numerical studies of linear instabilities have been reasonably successful in reproducing the characteristics of Gulf Stream meanders identified as unstable waves, and originating from the growth of wavelike disturbances from the mean state of the flow (Orlanski, 1969; Killworth, 1983; Killworth *et al.,* 1984; Johns, 1988; Barth, 1989a,b; Xue and Mellor, 1993; Feliks and Ghil, 1996; Boss *et al.,* 1996; Paldor and Ghil, 1997; Kontoyiannis, 1997). Simple idealized configurations employed in linear instability theories are 1-1/2 and 2 layer QG or shallow-water models with an upper layer, geostrophic front overlying a motionless lower layer and with a separating interface that can possibly outcrop to the sea surface. One of the main instability factors for a fixed potential vorticity front in the upper layer was found to be the relative thickness of the lower layer: Paldor (1983) showed that the front of a single layer with uniform potential vorticity is stable when the motionless lower layer is infinitely deep. Instabilities can also be generated in a reduced-gravity model with a geostrophic front where the potential vorticity is not constant (Killworth and Stern, 1982; Griffith *et al.,* 1982; Hayashi and Young, 1987; Paldor and Ghil, 1997). The instability criteria differ, depending on the model used: a change of sign in the basic state potential vorticity is required for instability in the QG-approximation (Pedlosky, 1987), while Killworth (1983) showed that instabilities in a primitive equation model can develop for a fast decaying infinite front where the potential vorticity slightly decreases toward the front. However, the calculated growth rates of the unstable modes in 1-layer models are much smaller than those derived from a 2-layer configuration (Phillips, 1954; Orlanski, 1969; Killworth *et al.,* 1984), or observed in laboratory experiments (Griffith and Linden, 1982; Chia *et al.,* 1982) all of which have an active lower layer. Killworth *et al.* (1984) showed that when the lower layer has a finite

vertical thickness, the geostrophic front destabilizes for any potential vorticity distribution. In general, the growth of the instabilities is significantly higher for a finite lower-layer depth, as their nature is mostly baroclinic, due to the vertical shear of the horizontal velocity. Studies of lateral boundary (e.g. coasts) effects have been carried out with a two-layer shallow-water model (i.e. Barth, 1989a,b) with different bottom topographies, and in a three-layer shallow-water model (Lee and Csanady, 1994), both using a vertical wall to represent a coastal boundary parallel to the outcropping front. In both studies, the wall reduces the instabilities' growth rates provided it is located within one radius of deformation from the surface front (i.e. the outcropping line of the lower layer).

In this work, we focus on the stabilization of a geostrophic surface front with constant potential vorticity in the vicinity (within a few radii of deformation) of a vertical wall in a two-layer shallow-water model with flat bottom. As in all previous studies the domain is bounded by a vertical wall so that the no-flow boundary condition is applied at the same location in both layers. The addition of the wall is the main difference between this study and the configuration studied by Killworth *et al.* (1984). Barth (1989a,b) has also included a coast in his instability calculations, but his eigenvalue problem was solved algebraically by crudely approximating derivatives by their finite difference analogue. Thus, the precision of Barth's method depends significantly on the spatial discretization of the equations so that higher accuracy can only be achieved by increasing the dimension of the matrix whose (complex) eigenvalues provide the sought growth rate. Instead, the differential shooting method employed in the present work is not restricted to coarse spatial resolution, which allows us to explore the more critical cases of relatively thin lower layers, and very long waves. As a result, we will show that some quantitative differences appear in the characteristics of the instabilities in the two methods. More significantly for depth ratios close to 1 the differences between the instability characteristics in the two methods are qualitative.

The paper is organized as follows: The formulation of the problem is described in Section 2. The numerical method used for solving the analytical equations are explained in Section 3a and the results are presented in Section 3b. Discussion of the results and comparison with Gulf Stream's observations are presented in Section 4 and summarized in Section 5.

2. Model

The configuration studied in this paper consists of a surface front in a 2-layer shallow-water model in an ocean with constant total depth, H, and with densities ρ_1 and $\rho_2 > \rho_1$ in the upper and lower layers, respectively. The upper layer has a geostrophic zonal mean flow $U(y)$ (cf Fig. 1) while the lower layer is motionless and it outcrops between the surface front (located along the $y = 0$ line) and a vertical wall located at a distance $y = L$ from the front. The purpose of this study is to investigate the development of linear instabilities of this set-up as an idealized scenario of the Gulf Stream (with the interface representing the thermocline) flowing at a certain distance (few radii of deformation) from
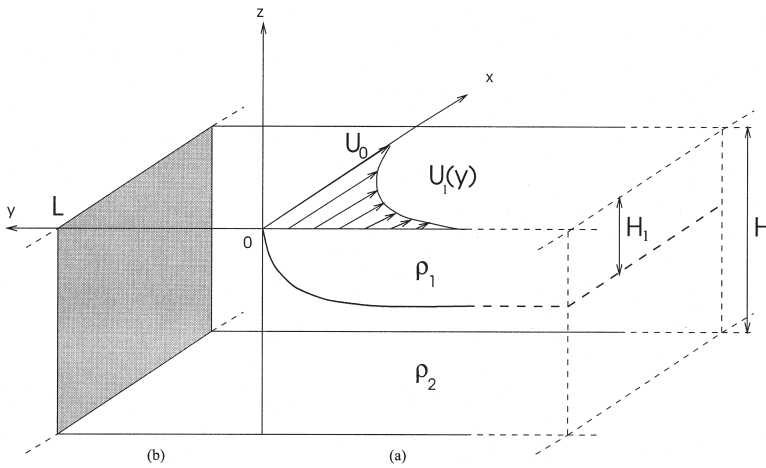
Figure 1. Model configuration, including a vertical wall at a distance $y = L$ from the geostrophic front where the lower layer outcrops.

the continental slope. Since in the Mid-Atlantic Bight west of the Gulf Stream the weak bottom slope beyond the depth of 4500 m is about two orders of magnitude smaller (10^{-4} versus 10^{-2}) than the continental slope, it is customary to simplify the topography below the open ocean as a flat bottom and to approximate the continental slope (upper 400 meter isobaths) as a vertical wall.

In each layer (denoted by the indices $i = 1, 2$), the momentum and continuity equations of the shallow-water model are:

$$\frac{\partial u_i}{\partial t} + u_i \frac{\partial u_i}{\partial x} + v_i \frac{\partial u_i}{\partial y} - f v_i = -\frac{1}{\rho_i} \frac{\partial p_i}{\partial x}$$

$$\frac{\partial v_i}{\partial t} + u_i \frac{\partial v_i}{\partial x} + v_i \frac{\partial v_i}{\partial y} + f u_i = -\frac{1}{\rho_i} \frac{\partial p_i}{\partial y} \tag{1}$$

$$\frac{\partial h_i}{\partial t} + h_i \left(\frac{\partial u_i}{\partial x} + \frac{\partial v_i}{\partial y} \right) + u_i \frac{\partial h_i}{\partial x} + v_i \frac{\partial h_i}{\partial y} = 0,$$

where u_i and v_i are the velocity components in the x and y directions respectively, ρ_i, p_i are the density and pressure, and f is the Coriolis frequency, treated here as a constant.

Typical velocities of 5–10 cm/s below the pycnocline are often neglected with respect to the 1 m/s average velocities (one order of magnitude higher) of an upper-layer jet like the Gulf Stream in idealized studies, such as the present one. The mean state is then chosen such that there is no mean flow in the lower layer, while the potential vorticity is constant in the upper layer, and equal to the ratio of f over H_1, which is the depth of the interface at $y = -\infty$.

By assuming a geostrophic balance, $\overline{u_2} = 0$, and constant potential vorticity in the upper layer, the solution for the mean state in the upper layer is therefore:

$$\overline{h_1}(y) = H_1(1 - e^{(y/R_d)}) \quad \text{with } y < 0, \tag{2}$$

where $R_d = \sqrt{g'H_1}/f$ is the internal radius of deformation, and $g' = g(\rho_2 - \rho_1/\rho_2)$ is the reduced gravity. Thus, $\overline{h_1}$ vanishes at the frontal line $y = 0$, and its exponential profile tends asymptotically to H_1 when $y \rightarrow -\infty$.

The expression of the geostrophic mean flow is then: $\overline{u_1}(y) = -(g'/f)(\partial \overline{h_1}(y)/\partial y) = fR_d e^{y/R_d}$, which has maximal value at $y = 0$ (outcropping point) and tends to zero at $y = -\infty$.

We nondimensionalize the governing equations by scaling the variables using f^{-1} as the time scale, H_1 as the scale for the layer thicknesses, and the internal radius of deformation, R_d, for x and y coordinates. The horizontal velocities are therefore scaled by (fR_d), and P/ρ is scaled on $|fR_d|^2$.

This choice of scaling leads to simple expressions of the nondimensional mean state in the upper-layer:

$$\overline{h_1}^* = 1 - e^{y^*}$$
$$\overline{u_1}^* = e^{y^*}, \tag{3}$$

where * designates nondimensional variables.

Now, a nondimensional perturbation component a'^* of zero-mean is added to each of the mean flow variables $\overline{u_i}^*$, $\overline{v_i}^*$, $\overline{h_i}^*$, such that $a'^* \ll \overline{a}^*$, so any flow variable a^* is in approximate geostrophic balance.

We then linearize the governing equations about the basic state described above and after simplification of the notation by dropping the stars from all nondimensional variables and primes from the nondimensional perturbation variables, we get the following system of nondimensional equations in the region $y \leq 0$:

$$\frac{\partial u_1}{\partial t} + \overline{u_1}\frac{\partial u_1}{\partial x} + v_1\frac{\partial \overline{u_1}}{\partial y} - v_1 = -\frac{\partial p_1}{\partial x}$$

$$\frac{\partial v_1}{\partial t} + \overline{u_1}\frac{\partial v_1}{\partial x} + u_1 = -\frac{\partial p_1}{\partial y}$$

$$\frac{\partial(p_1 - p_2)}{\partial t} + \overline{h_1}\left(\frac{\partial u_1}{\partial x} + \frac{\partial v_1}{\partial y}\right) + \overline{u_1}\frac{\partial(p_1 - p_2)}{\partial x} + v_1\frac{\partial \overline{h_1}}{\partial y} = 0$$

$$\frac{\partial u_2}{\partial t} - v_2 = -\frac{\partial p_2}{\partial x} \tag{4}$$

$$\frac{\partial v_2}{\partial t} + u_2 = -\frac{\partial p_2}{\partial y}$$

$$-\frac{\partial(p_1 - p_2)}{\partial t} + (r - \overline{h_1})\left(\frac{\partial u_2}{\partial x} + \frac{\partial v_2}{\partial y}\right) - v_2\frac{\partial \overline{h_1}}{\partial y} = 0$$

where $r = H/H_1$ (≥ 1) is the depth ratio, $h_1 = p_1 - p_2$ (hydrostatic approximation), and $h_2 = -h_1$ (rigid-lid approximation).

In the region $0 \leq y < L$ only the lower layer exists so the shallow-water equations in this region are:

$$\frac{\partial u_2}{\partial t} - v_2 = -\frac{\partial p_2}{\partial x}$$

$$\frac{\partial v_2}{\partial t} + u_2 = -\frac{\partial p_2}{\partial y} \tag{5}$$

$$\frac{\partial u_2}{\partial x} + \frac{\partial v_2}{\partial y} = 0.$$

It is assumed now that the perturbation fields have an oscillatory behavior of a wave-like dependence in time and zonally, such that:

$$(u_1, v_1, p_1, u_2, v_2, p_2) = (U_1(y), V_1(y), P_1(y), U_2(y), V_2(y), P_2(y))e^{ik(x-ct)}, \tag{6}$$

where $u_1, v_1, p_1, u_2, v_2, p_2$ are the six nondimensional perturbation variables, $U_1(y)$, $V_1(y)$, $P_1(y)$, $U_2(y)$, $V_2(y)$, $P_2(y)$ are their corresponding amplitudes, k is the wavenumber of the perturbation, and $c = c_r + ic_i$ is the phase speed.

A substitution of Eq. (6) into the governing equations in both spatial domains (Eqs. (4) and (5)) eliminates the x and t derivatives of the perturbation variables, which simplifies the equations as follows:

In region (a) ($y < 0$):

$$\left[k^2(\overline{u_1} - c)^2 + \frac{\partial \overline{u_1}}{\partial y} - 1 \right] V_1 - ik(\overline{u_1} - c)\frac{\partial P_1}{\partial y} + ikP_1 = 0,$$

$$\overline{h_1}\frac{\partial V_1}{\partial y} + \left[k^2\overline{h_1}(\overline{u_1} - c) + \frac{\partial \overline{h_1}}{\partial y} \right] V_1 - ik\overline{h_1}\frac{\partial P_1}{\partial y} + ik(\overline{u_1} - c)(P_1 - P_2) = 0,$$

$$(1 - k^2c^2)V_2 - ikc\frac{\partial P_2}{\partial y} - ikP_2 = 0 \tag{7}$$

$$(r - \overline{h_1})\frac{\partial V_2}{\partial y} - \left[\frac{\partial \overline{h_1}}{\partial y} + k^2c(r - \overline{h_1}) \right] V_2 - ik(r - \overline{h_1})\frac{\partial P_2}{\partial y} + ikc(P_1 - P_2) = 0,$$

and in region (b) (i.e. $0 \leq y < L$):

$$-ikc\frac{\partial P_2}{\partial y} + (1 - k^2c^2)V_2 - ikP_2 = 0,$$

$$\frac{\partial V_2}{\partial y} - \frac{V_2}{c} + \frac{ik}{c}P_2 = 0. \tag{8}$$

The reduction in the number of unknowns from 6 to 4 in region (a) and from 3 to 2 in region (b) is achieved by eliminating the perturbation amplitudes $U_1(y)$ (in region (a)) and $U_2(y)$ (in both regions), using the x-momentum equations.

It is always preferable to integrate differential equations over a finite domain instead of an infinite domain. Toward that end, we change the independent variables from y to $z = e^y$ so that $0 < z < 1$ in region (a) while $1 < z < z_o = e^l (=e^{L/R_d})$ in the region (b).

The governing equations in region (a) now become:

$$z \frac{\partial P_1}{\partial z} = \left[\frac{1-z}{z-c} - k^2(z-c) \right] V_1 + \frac{1}{z-c} P_1,$$

$$z \frac{\partial V_1}{\partial z} = \left[\frac{z}{1-z} - \frac{1-z}{z-c} \right] V_1 + \left[\frac{z-c}{1-z} - \frac{1}{z-c} \right] P_1 - \frac{z-c}{1-z} P_2,$$

$$cz \frac{\partial P_2}{\partial z} = -P_2 - (1 - k^2 c^2) V_2,$$

$$cz \frac{\partial V_2}{\partial z} = \left[1 - \frac{zc}{r-1+z} \right] V_2 + \frac{c^2}{r-1+z} P_1 + \left[1 - \frac{c^2}{r-1+z} \right] P_2,$$

$$(9)$$

and in region (b) the governing equations become:

$$cz \frac{\partial P_2}{\partial z} = -(1 - k^2 c^2) V_2 - P_2,$$

$$cz \frac{\partial V_2}{\partial z} = V_2 + P_2,$$

$$(10)$$

(the imaginary number i was eliminated by replacing V_j by $(i/k)V_j$ in each layer).

The equations must then satisfy the following boundary conditions:

- At the wall ($z = z_o$), V_2 must vanish for all r, l, k, c.
- At $z = 1$ (the location of the surface front, which separates the two regions) the lower layer solutions for V_2 must be continuous in the lower-layer velocity fields (but their derivatives are discontinuous at $y = 0/z = 1$).
- At $z = 0$ (i.e. $y = -\infty$), all eigenfunctions are finite. Note that for $r > 1$, the singularity of the equations at $z = 0$ is removable but for $r = 1$, this singularity is nonremovable.

3. Solution and results

a. Method of solution

In region (b) explicit solutions for V_2 and P_2 in Eq. (10) exist which can be expressed as a linear combination of z^k and z^{-k}. These explicit solutions introduce the dependence

of the solutions on L (the dimensional distance between the wall and the surface front) by imposing a boundary condition on the solutions in region (a). The explicit solutions in region (b) are:

$$P_2 = M z_o^k \left[(kc - 1) \left(\frac{z}{z_o} \right)^k + (kc + 1) \left(\frac{z}{z_o} \right)^{-k} \right]$$

$$V_2 = M z_o^k \left[\left(\frac{z}{z_o} \right)^k - \left(\frac{z}{z_o} \right)^{-k} \right] = \frac{1}{kc \coth (k(y - l)) - 1} P_2 \tag{11}$$

where M is an arbitrary constant and the last equality in V_2 was added only in order to clarify its structure in the cartesian, dimensional, coordinates y and L.

The singularities at the lateral boundaries of region (a) ($z = 0$ and $z = 1$) are now considered in order to integrate the solutions:

Near $z = 0$ ($y \to -\infty$), in order for the z-derivatives to be bounded and nontrivial, the perturbations' amplitudes must have a power series expansion in z:

$$(V_1, P_1, V_2, P_2) \approx (\widetilde{V_1}, \widetilde{P_1}, \widetilde{V_2}, \widetilde{P_2}) z^\beta, \tag{12}$$

with $Re(\beta) > 0$.

We substitute this expansion into the governing equations in region (a) for $z \ll 1$, which leads to the single quadratic equation for β^2:

$$c^2 - \frac{r-1}{c^2} \left[\frac{1 - \beta^2 c^2}{1 - k^2 c^2} + c^2 - 1 \right] \left[\frac{1 - \beta^2 c^2}{1 - k^2 c^2} + \frac{c^2}{r-1} - 1 \right] = 0. \tag{13}$$

Realizing that one of the roots of this equation is ($\beta_1^2 = k^2$) enables us to put this equation in its canonical form and deduce the second root, which is:

$$\beta_2^2 = k^2 + (1 - k^2 c^2) \frac{r}{r-1}. \tag{14}$$

Thus, there exist two independent vectors of solutions near $z = 0$, i.e. for $z = \epsilon \ll 1$:

$$P_1(\beta_1) = \widetilde{P_2} \epsilon^k,$$

$$V_1(\beta_1) = -\frac{1}{1 - kc} \widetilde{P_2} \epsilon^k, \tag{15}$$

$$V_2(\beta_1) = -\frac{1}{1 - kc} \widetilde{P_2} \epsilon^k = V_1(\beta_1),$$

and

$$P_1(\beta_2) = -(r - 1)\widetilde{P_2}\epsilon^{\beta_2},$$

$$V_1(\beta_2) = \frac{(r - 1)\left(1 + c\sqrt{k^2 + (1 - k^2c^2)\dfrac{r}{r - 1}}\right)}{1 - k^2c^2}\widetilde{P_2}\epsilon^{\beta_2}, \tag{16}$$

$$V_2(\beta_2) = -\frac{\left(1 + c\sqrt{k^2 + (1 - k^2c^2)\dfrac{r}{r - 1}}\right)}{1 - k^2c^2}\widetilde{P_2}\epsilon^{\beta_2} = -\frac{V_1(\beta_2)}{r - 1},$$

where $\widetilde{P_2}$ is an arbitrary constant.

Near $z = 1$, the differential equation for V_1 in system (9) reduces to:

$$(1 - z)\frac{\partial V_1}{\partial z} \approx V_1 + (1 - c)P_1 - (1 - c)P_2, \tag{17}$$

which cannot be solved explicitly. However, for finite $\partial V_1/\partial z$ this equation provides a relationship between V_1 and the perturbation pressures P_1 and P_2 at $z \approx 1$. Consequently, near $z = 1$ the other variables and their first derivatives can also be expressed as functions of P_1 and P_2 only:

$$\frac{\partial P_1}{\partial z} = \left[\frac{1}{1 - c} - k^2(1 - c)^2\right]P_1 - k^2(1 - c)^2P_2,$$

$$V_1 = (1 - c)[P_2 - P_1],$$

$$\frac{\partial P_2}{\partial z} = \left[\frac{1 - k^2c^2}{kc\,\coth\,(kl) + 1} - 1\right]\frac{P_2}{c}, \tag{18}$$

$$V_2 = -\frac{P_2}{kc\,\coth\,(kl) + 1},$$

$$\frac{\partial V_2}{\partial z} = \frac{c}{r}P_1 + \frac{1}{r}\left[\frac{1}{kc\,\coth\,(kl) + 1} + r - c^2\right]P_2$$

(Note that coth(kl) is short for $(z_0^k + z_0^{-k})/(z_0^k - z_0^{-k})$. Instabilities in the mean flow described above appear when the phase speed of the wave-like disturbance is complex, with a nonzero imaginary component. The temporal growth of these instabilities is exponential and is characterized by the exponent kc_i. Complex phase-speeds of the perturbations are obtained as the complex eigenvalues of the eigenvalue problem system, which is solved numerically using the shooting method.

The shooting algorithm for solving the eigenvalue problem consists of the following steps: Since an explicit solution was found in region (b) (i.e. $l \geq y \geq 0$) numerical integration of the differential equations is only required in region (a). The integrations start

at the boundaries of region (a), $z = \epsilon$ and $z = 1$, where the z-dependence of the well-behaved solutions in this region is already known. At $z = \epsilon$, the integration is initiated with the two independent vectors of solutions (one for each value of β), by assigning the arbitrary amplitude, $\widetilde{P_2}$, the value of 1 in each of the two integrations (one integration for each allowable value of β). The complete solution for $\epsilon < z < 1$ is a linear combination of the two solutions found by these two numerical integrations. At $z = 1$, we recall that the value of $P_1(1)$ is not determined while the value of $P_2(1)$ should equal (by continuity) its corresponding value in region (b), which is an undetermined constant of integration there. The general solution at $z = 1$, therefore, is a linear combination of two independent solutions: The first has ($P_1 = 1$; $P_2 = 0$) and the second with ($P_1 = 0$; $P_2 = 1$).

To find numerically the complete solution in the range $0 \leq z \leq 1$, we begin by carrying out two numerical integrations starting at $z = 1$, with the general solution at $z = 1$ as described above and ending at $z = 0.5$. The values ($P_1(z = 0.5^+)$, $P_2(z = 0.5^+)$, $V_1(z = 0.5^+)$, $V_2(z = 0.5^+)$) that result from these two integrations are stored. Two additional sets of numerical integrations are carried out from $z = 0$ to $z = 0.5$, starting with the well-behaved solution near $z = 0$ as described above. The general solution in $0 \leq z \leq 0.5$ is also a linear combination of these two solutions and the values of ($P_1(z = 0.5^-)$, $P_2(z = 0.5^-)$, $V_1(z = 0.5^-)$, $V_2(z = 0.5^-)$) that result from these two additional integrations are also stored. Requiring that the solution for ($P_1(z)$, $P_2(z)$, $V_1(z)$, $V_2(z)$) be continuous at $z = 0.5$ provides the final condition that determines the phase speed, $c = c_r + ic_i$ as follows.

For fixed values of the parameters of the problems (l, k, r), we calculate the determinant of the four values of P_1, P_2, V_1, V_2 at $z = 0.5$, that results from the four integrations described above. We then search for the complex value of $c = c_r + ic_i$ at which the determinant vanishes. This value is the sought unstable phase speed and the corresponding eigenfunctions are the nontrivial continuous solution of (P_1, P_2, V_1, V_2) in the entire $0 \leq z \leq 1.0$ interval. For the initial guess of (c_r, c_i), where the search for the eigenvalue begins, we chose the values calculated in Barth (1989b) for ($l = 2, r = 2, k = 1$), from which we searched for (c_r, c_i) by varying (l, k, r) in small increments.

b. Results

A large number of growth rate computations were carried out for the same $U_o(H_1)$ profile by varying the values of the 3-model parameters: The depth-ratio $r = H/H_1$, the distance between the outcropping front and the wall $l = L/R_d$, and the perturbation's zonal wavenumber k.

The resulting dispersion curves $\sigma_i(k) = k \times c_i(k)$ for several values of the depth ratio, r, in the range $r = 1.001 - r = 20$ are shown in Figure 2. In the range of r between 1.5 and 20, the growth rate curves exhibit similar characteristics for all values of r: A single local maximum growth rate, which defines the most unstable wave corresponding to wavenumber k_{max}, followed by a decrease in growth rate and ending abruptly at a
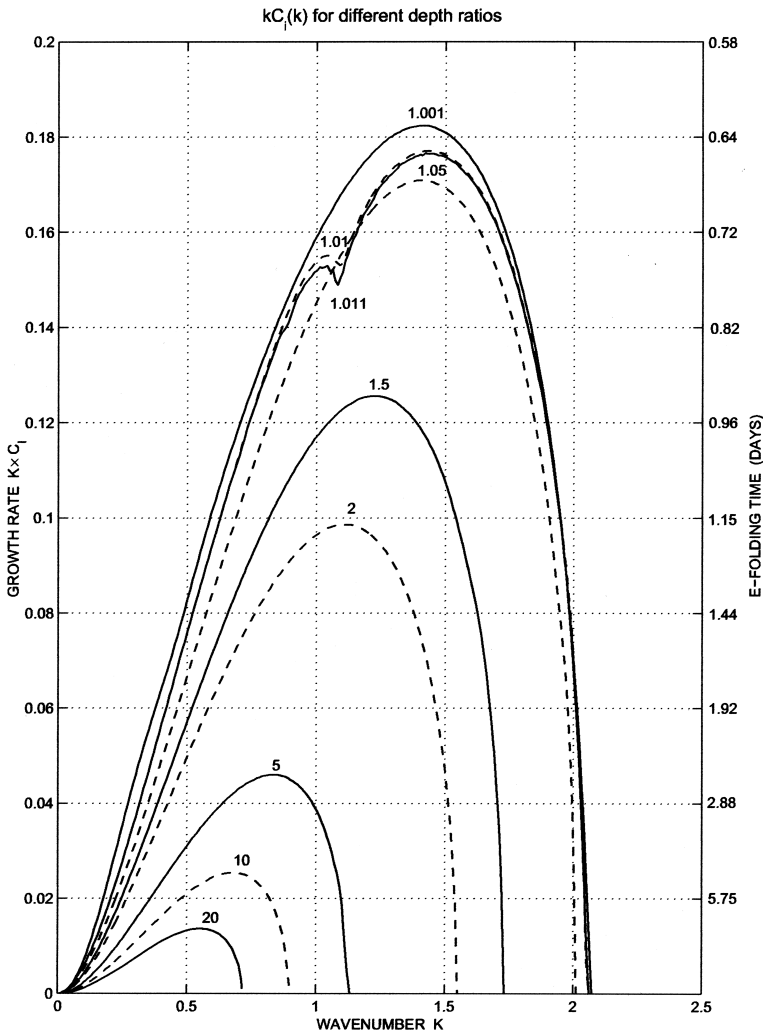
Figure 2. Growth rate $\sigma_i = kc_i$ and corresponding e-folding times for $l = 2$, as a function of k for different depth ratios r, including $r = 1.011$, and 1.001.

shortwave, k_c. For wavenumbers smaller than k_{max}, σ_i decreases smoothly toward zero at the infinite wavelength limit (i.e. $k = 0$). For $r - 1 \ll 1$, on the other hand, not only do the maximal growth rates increase significantly, but a second local maximum exists.

Note, however, that the application of the shooting method at small wavenumbers and at depth ratios very close to 1 has increased uncertainty due to the singularity of the differential equations in these two limits. Nevertheless, the general trend in the σ-curve indicates a convergence to zero as k tends to zero, as do the $c_i(k)$ curves in Figure 3b. For k larger than the critical wavenumber, k_c (which depends on r), the unstable mode ceases to
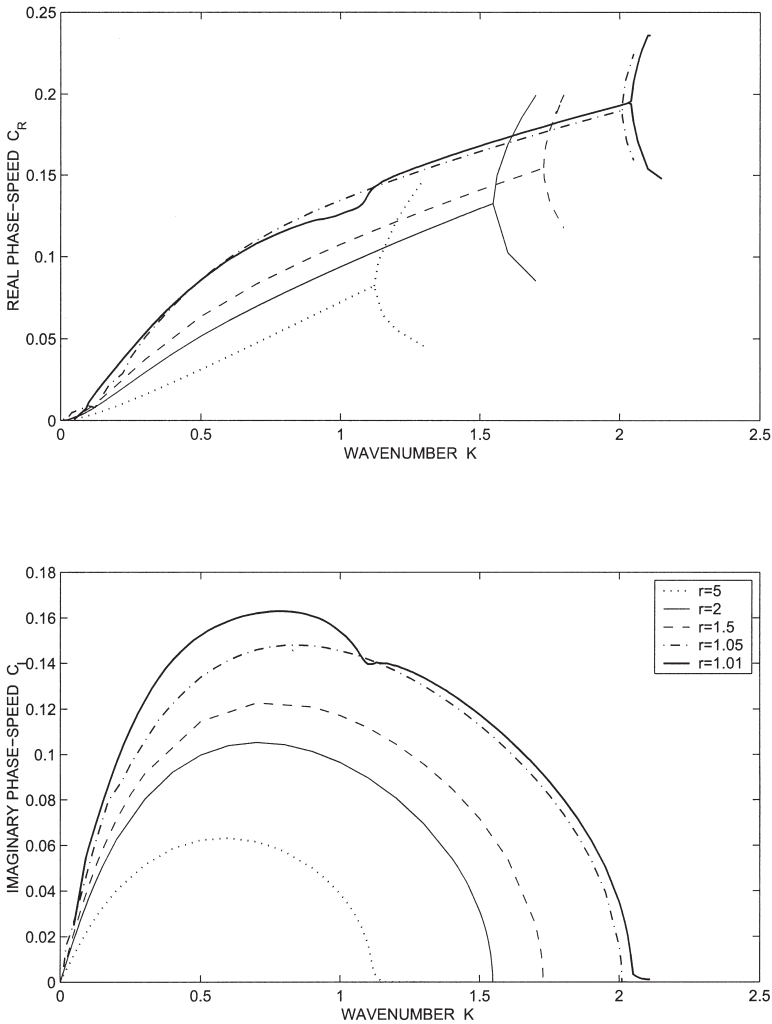
Figure 3. Real (c_r) and imaginary (c_i) phase speeds for 5 different depth ratios.

exist and the $c_r(k)$ curve bifurcates into two real modes, as shown in the real phase speed curves in Figure 3a. This shortwave cut-off and mode splitting at the bifurcation wavenumber k_c typifies most frontal instability curves (e.g. Killworth *et al.,* 1984; Barth, 1989b; Paldor and Ghil, 1991, 1997) and indicates that the instability originates from the coalescence of two real modes.

Our main interest is in the effect of the depth-ratio on the existence and development of the linear instabilities, especially when it gets small. The growth rate and dispersion relationship derived from this method for $r \geq 2$ are in very reasonable agreement with the results of Barth (1989b), and only slight discrepancies exist—the wavenumber of maxi-

mum growth rate, k_{max}, is slightly different (i.e. 1.05 vs 1.1) and the shortwave cutoff, k_c, is slightly higher in our calculations. The main effect of decreasing the depth ratio is to significantly increase the growth rate, phase speed, and wavenumber of the fastest growing wave k_{max}, i.e. reducing the wavelength of the most unstable wave. Values of the growth rate range from 0.014 for $r = 20$ to 0.125 for $r = 1.5$ (which corresponds dimensionally to an e-folding time of 8.2 days for $r = 20$, to 0.9 day for $r = 1.5$). The wavenumber of maximal growth rate, k_{max}, ranges from 0.6 for $r = 20$ to 1.2 for $r = 1.5$. This behavior is known to be related to the higher vertical shear of the mean flow over the entire water column when the lower-layer thickness becomes shallower, which leads to instabilities developing and propagating much faster at a shorter dominant wavelength.

In contrast to the earlier studies, we have also investigated the range of $1 < r < 2$, corresponding to relatively thin (and even nearly vanishing) lower layers. Instabilities in this range of depth ratio cannot be studied in the QG approximation since the relative change in the height of the lower layer cannot be assumed small even when the Rossby number is sufficiently small. Near $r = 1.01$, there is a second local maximum at $k \approx 1.05$. Other experiments for nearby values of r indicate that the change in the curve's monotony is sharpest for $r = 1.01$. This result is similar to other studies on linear instabilities (e.g. Paldor and Ghil, 1991), and can be explained by the interaction of the unstable mode with a third mode. The resonance of this mode occurs for $1.005 \leq r < 1.05$. Note also in Figure 3 how the real phase speed is affected for $r = 1.01$ with respect to $c_r(r = 1.05)$ near $k = 1.05$.

In order to understand the relationship between the frequency and phase speed as a function of r, we fitted simple functions to the results of Figures 2 and 3. In Figure 4a, we show some of the results of Figures 2 and 3 but this time plotted on a logarithmic scale versus $ln(r)$ (note that the origin of the abscissa corresponds to $r = 1$). The following fitting functions were found for σ_{imax}, k_{max}, k_c and c_r by finding the linear best-fit of the logarithmic curves:

For $1.001 \leq r \leq 20$:

$$\sigma_{imax} \approx 0.183 r^{-0.87}$$

$$k_{max} \approx 1.408 r^{-0.317}$$

$$k_c \approx 2.034 r^{-0.357} \tag{19}$$

$$c_r \approx 0.162 r^{-0.63}.$$

These fitting functions provide an easy estimate for the four observable variables as functions of r and highlight the importance of the lower layer thickness (relative to that of the upper layer) in the dynamics of linear instabilities—the four variables all vanish when the lower layer becomes infinitely thick ($r \to \infty$). Note that although formally, all four variables are singular (approach ∞) when r approaches 0, this formal limit has no physical meaning since, by definition, $r > 1$. A similar result was found by Oey (1988) using a nonlinear, time-dependent, three-dimensional model. His configuration is similar to ours in
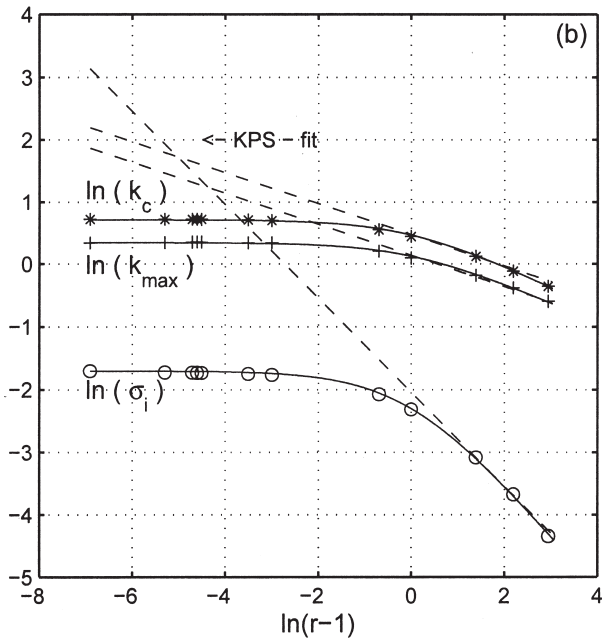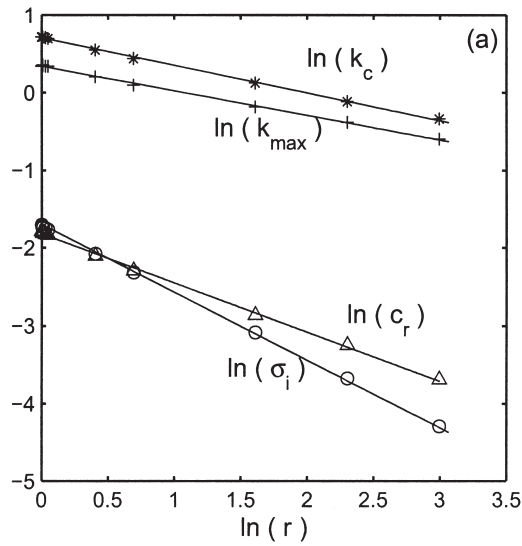
Figure 4. (a) Fitting functions of σ_i (circle), k_{max} (cross), c_r (triangle) and k_c (star) versus $ln(r)$. (b) Fitting functions of σ_i, k_{max} and k_c versus $ln(r - 1)$, superimposed on the fitting functions of Killworth *et al.* (1984) (dashed lines).
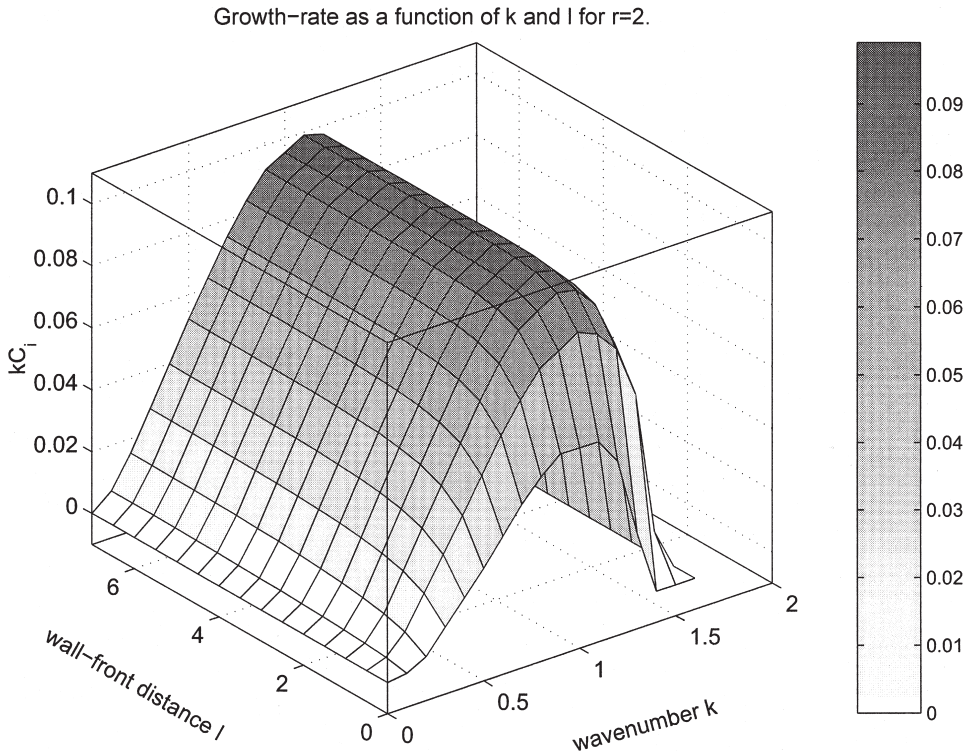
Growth−rate as a function of k and l for r=2.

Figure 5. Growth rate as a function of the wavenumber k and distance from the wall l for a depth ratio of $r = 2$.

that he has an outcropping front and vertical wall. However, his study deals with a rectangular channel with periodic boundary conditions. Oey concludes that when the distance of the wall from the front is larger than one radius of deformation (i.e. $l > 1$ in our notation) the growth rate varies with r as r^{-n} where $n < 1$. In comparison in the present study, our results for the maximum growth rate, σ_{imax} have $n = 0.87$ in Oey's notation.

This close analogy between our results, which obtain as solutions of a linear eigenvalue problem, and the nonlinear, 3-dimensional, results of Oey (1988) is not unique. Similar analogy was also encountered in previous works (e.g. Boss and Thompson, 1999) where quantitative estimates (e.g. wavelength with maximal growth rate) derived from linear and quasi-linear instability theories (which formally apply only to the initial stages of the perturbations' growth) turned out to provide reasonable estimates for the unstable waves' characteristics (i.e. length scale) even at mature stages of growth (e.g. long time into the development of meanders), when nonlinear effects become important and linear results are not expected to be relevant.

The influence of the wall on the development of instabilities is illustrated in Figure 5, where we plot the growth rate as a function of both l ($=L/R_d$) and k, and the results are
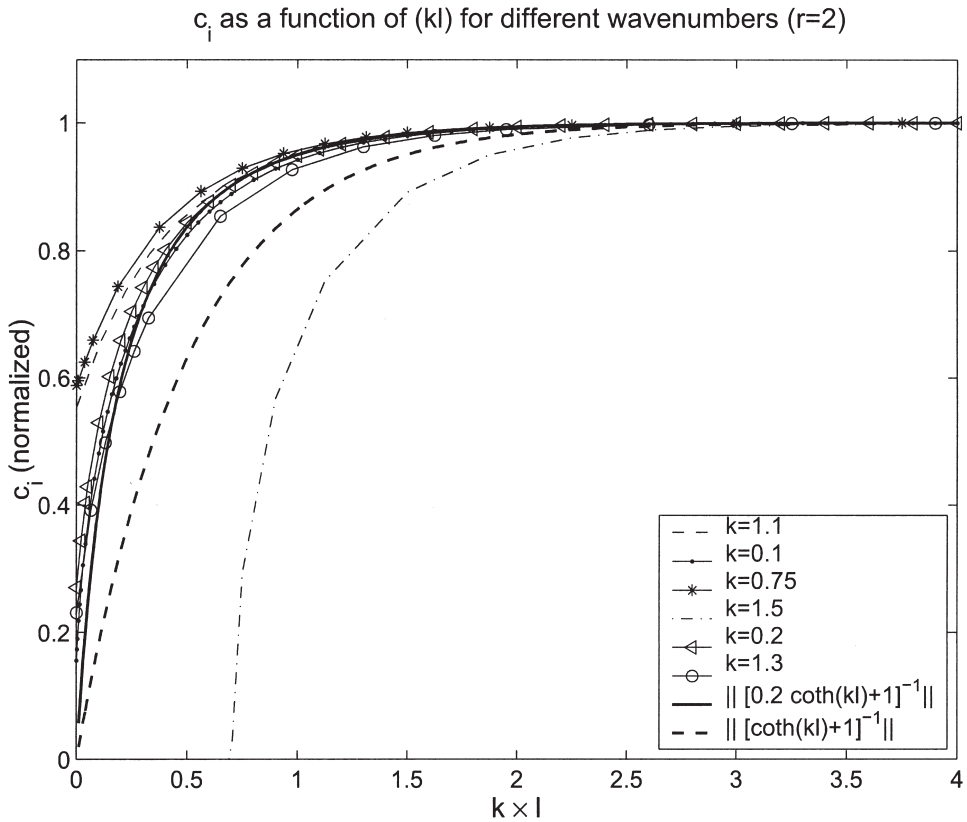
Figure 6. Imaginary phase speed c_i normalized by its asymptotic value for large l, plotted as a function of the quantity $(k \times l)$.

qualitatively similar to those of Barth (1989). For $l \geq 2$ (i.e. $L \geq 2R_d$), c_i is asymptotic to a constant value (that depends on k), hence the "wall effect" is felt only within about 1 radius of deformation from the outcropping front. Note also at $l = 0$ the slower rate of decrease in σ_i when k tends to k_c. The proximity of the wall appears to have only a slightly stabilizing effect on the unstable waves as even at $l = 0$, the growth rate decreases only to more than one half of its asymptotic, large l, value. This behavior seems to be due to the introduction of l in the hyperbolic cotangent expression $1/(kc \coth (kl) + 1)$ in the boundary conditions of the lower layer at $z = 1$, as l does not appear anywhere else in the governing equations. The primary dependence on this term becomes obvious when plotting c_i versus kl for different wavenumbers (i.e. Fig. 6): The cotangent function reaches its asymptotic value for $kl \approx 2$ as do all c_i curves. Therefore, the wall affects the resulting instability curves only via its presence in the $\coth (kl)$ term of the boundary condition of the lower layer in region (a), which is negligible when the wall is located more than two radii of deformation away from the surface front. Oey (1988) relates the decrease in growth

rate when $L < R_d$ to the reduced effect of rotation, which results in more available potential energy being converted to mean kinetic energy. Since the growth rate of baroclinic instability depends on the available potential energy, via its conversion into eddy kinetic energy (Cronin and Watts, 1996), less energy is available for conversion into eddy kinetic energy, which is reflected in the decrease in the instabilities' growth rate.

4. Discussion

a. Comparison with Barth (1989)

Our physical set-up (flat bottom, vertical wall, constant potential vorticity in the upper layer and motionless lower layer) is the same as that studied in Barth (1989b), and for the most part when the parameter values overlap the results of the two studies are very similar (both quantitatively and qualitatively). However, the numerical methods employed in the two studies are different: Barth solves the eigenvalue problem by discretizing in the entire infinite y-range over a finite subinterval. This method suffers from two inaccuracies: The first is that the behavior of the eigenfunctions at $y = -\infty$ (imposed here as the boundary conditions at $z = 0$) cannot be handled accurately and is replaced by imposing vanishing of the eigenfunctions at some large, but finite, y. The second is that the spatial resolution associated with any finite difference analog of an eigenvalue differential equation limits the accuracy since higher resolution in y (to increase the spatial resolution) comes at the expense of an increase in the dimension of the matrix whose (algebraic) eigenvalues are to be computed. The larger the matrix is, the more difficult it becomes to diagonalize the matrix and calculate the particular complex eigenvalue that yields the instabilities' growth rate. In contrast, the method of solution employed in the present study consists of integrating the differential equations with very high accuracy (the 5th order Runge-Kutta integration scheme we used had a 10^{-13} accuracy) and calculating the determinant of a 4×4-matrix of the constants of linear combination of the four numerical integrations. A determinant of dimension 4 only can be calculated very accurately, even when its elements are complex, so the resulting value of $c = c_r + ic_i$ at which the determinant vanishes is very accurate. The transformation of the independent coordinate y, which varies over the infinite domain of $[0, -\infty)$ into the $z = e^y$, which varies over the $[0, 1]$ domain, further simplifies the integration of the differential equations and enables an accurate determination of the phase speed. The higher spatial resolution in our study may explain the slight differences in k_{max} and k_c between Barth's numbers and ours: for a depth-ratio value of 2, we find a maximum growth-rate of 0.099, which is 9% higher than Barth's value. Similarly, the difference for k_{max} and k_c are of the order of 3–4%, while the real phase speed values are identical. The difference between the values of σ_{imax} for $r = 5$ is reduced to 4.3%, and it becomes insignificant for the higher depth ratios.

It seems, therefore, that the resulting discrepancies between the two methods are negligible for large $r - 1$, but become important (mostly in σ_i and k_{max}) for $r - 1 \leq 1$. One might assume that the differences in the growth rate and most unstable wavenumber

Table 1. Analytical solutions and fitting functions of r for σ_{imax}, k_{max} and k_c.

Ref.	σ_{imax}	k_{max}	k_c
This study ($1.001 \leq r \leq 20$)	$0.183r^{-0.87}$	$1.408r^{-0.317}$	$2.034r^{-0.357}$
KPS (1984) ($2 \leq r \leq 20$)	$0.13(r-1)^{-0.75}$	$1.15(r-1)^{-0.25}$	$1.6(r-1)^{-0.25}$
Phillips (1954)	$0.88(r-1)^{-3/4}$	$(4/3)^{1/4}(r-1)^{-1/4}$	$2^{1/2}(r-1)^{-1/4}$

keep increasing as $r - 1$ tends to zero, but the smallest depth ratio investigated by Barth is $r = 2$.

b. Comparison with Killworth et al. (1984)

Killworth *et al.* (1984) studied the development of wavelike instabilities in a physical set-up that is very close to ours (uniform vorticity in the upper layer, motionless lower layer, outcropping interface) with the exception of the vertical wall. Instabilities occur in their study when a slightly variable potential vorticity is added to the potential vorticity in the upper layer. Their analytical results are derived for long waves and deep lower layers, and these expressions are confirmed and then extended to finite wavelengths and moderately deep lower layers, numerically. The main finding in their study is the fitting functions for k_{max}, σ_{imax} and k_c, which are expressed in the form of $(r - 1)^a$, with $a < 1$. These functions are comparable to the Phillips (1954) quasi-geostrophic model applied to a flow unbounded in y (cf Table 1). It is clear from the results shown in Table 1 that in the limit when the upper layer extends to the ocean's bottom, $r \to 1$, this form of the fitting functions leads to diverging σ_{imax}, k_c and k_{max}. This is in contrast to our results which are asymptotic to a finite value at $r = 1$ and the growth rate does not increase as dramatically when $r \to 1$. Although their results of $\sigma_{imax} = 0.13(r - 1)^{-3/4}$ are in reasonable agreement with ours for $r > 2$, our results (cf Fig. 4b) are fundamentally different for $1.001 \leq r \leq 2$. Our accurate method of solution enabled us to cover a wider set of small depth ratios by including the cases of relatively thin to vanishing lower layers, which allowed us to investigate the solution of the system in a parameter range not considered in previous studies. This led to new fitting functions for the maximal growth rates and wavenumbers.

We looked at the results of Killworth *et al.* (1984) and ours for $l = 2$. However, most variables are close enough to their asymptotic values to validate the comparison. The significant difference in the behavior of the fitting curves in the depth-ratio range $1 \leq r \leq 2$ compared to that in $r > 2$ raises a doubt on the applicability of QG models when the lower (motionless) layer is thinner than the upper layer (where the mean flow occurs).

c. Comparison with Gulf Stream's observations

The 2-layer, shallow-water, configuration of the present study has been frequently employed to study the dynamics of major ocean currents such as the Gulf Stream, where the velocity is negligible below the main thermocline. In the mean, the Gulf Stream can be

accurately approximated by a geostrophic surface front of constant potential vorticity with a path nearly parallel to the continental slope, represented here by the vertical wall. The distance between the Stream (i.e. its North Wall) and the continental slope varies between 1–3 R_d south of Cape Hatteras and about 10 R_ds downstream of the New England Seamount Chain. In the latter region, the radius of deformation is roughly from 30 to 50 km. By dimensionalizing the results accordingly and taking a typical depth ratio of $r = 5$ (corresponding to a total depth of 500 meters and a main thermocline depth of 1000 meters), we find that the fastest growing meanders have a period of 18 days, and an e-folding time of 2.5 days. The wavelength ranges from 260–360 km depending on the value chosen for the radius of deformation so the propagation phase speed ranges from 14 to 22 km day^{-1}. The dimensional values of the most unstable waves for different depth ratios are shown in Table 1 (wavelength and phase speed values were calculated for a deformation radius of 40 km). These unstable waves seem to fall in the category of fast growing meanders of 200–400 km with relatively small periods and short e-folding times of the order of 1 to 5 days, which are characteristics of baroclinic and mixed barotropic-baroclinic instabilities, generated by the vertical shear of the horizontal velocity.

The most relevant observations for the Gulf Stream's typical depth-ratio range ($2 \leq r \leq 5$), are from Kontoyiannis and Watts (1994), and Tracey and Watts (1986) who used arrays of inverted echo sounders to monitor the path of the Stream. In both studies, similar values to within a factor of 2 were found downstream of Cape Hatteras. Their measured period was below 8 days and the e-folding times are 3–4 days, which are close to our calculated values for the most unstable waves for r in this range of 2 to 5. Other observations reported by Watts and Johns (1982) have also identified meanders of rapid growth (e-folding time ~6 days), but with wavelengths of 400 km and above, which fit the unstable mode of the present study but for a depth ratio of 10.

South of Cape Hatteras, the Gulf Stream flows in the mean along the upper continental slope and shelf-break. Depending on its lateral oscillations, its signature either extends all the way to the bottom, or is intersected by the presence of the Deep Western Boundary Current, where the velocity is not negligible. Thus, the idealized configuration used in this study is not applicable to the Gulf Stream's meandering activity upstream of Cape Hatteras.

One has to keep in mind the simplicity of this idealized configuration, where part of the continental slope is approximated as a vertical wall, whereas the offshore part is considered as a flat bottom. While the wall's influence on the stability of the front becomes insignificant beyond a distance of 1–2 R_d, the existence of a bottom slope was shown to have a significant effect on the growth rate (Barth, 1989; Johns, 1988), both by reducing its maximal value dramatically and shifting the most unstable waves to longer wavelengths. Johns (1988) showed that for bottom slopes of the order of the continental slope in the North Atlantic Bight, increasing the bottom slope by a factor of 4 causes a decrease in the instabilities' growth-rate (in the long-wave range) by a factor of 3. Similarly, Barth (1989b) showed that a bottom slope of $0.5 \times H_1/R_d$ decreases the growth rate by a factor

Table 2. *e*-folding time, wavelength, phase speed and period of the most unstable wave calculated for a radius of deformation of 40 km, and meander characteristics from Gulf Stream's observations.

Depth ratio $r = H/H1$	*e*-folding time (days)	Dominant wavelength λ (km)	Phase speed c_r (km · day^{-1})	Period T (days)
10	4.3	370	14	27
5	2.5	300	20	16
2	1.2	230	35	8
1.5	0.9	203	43	4.7
1.05	0.6	175	55	3
Observations				
Brooks and Bane (1981)	—	100–200	30–40	3, 7–8
Watts & Johns (1982)	4.5–6	≥400	20–30	≥14
	5.5–7.5	≤184	~40	~4.5
Tracey & Watts (1986)	7–8	180–230	45–46	4–5
Kontoyiannis & Watts (1994)	2–4	230–260	31–35	6.5–8.5
	3.5–6	212	41	5.2
	5.5–12	195	46	4
	3.5–10	180	51	3.6
Lee & Cornillon (1996)	—	320	13.3	20–30
	—	270	20.2	10–20
	—	223	27.0	7–10
	—	197	38.8	4–7

of 6–7. The upper continental slope can be approximated by a linearly sloping bottom with a slope of about 10^{-2}. Hence, for a deformation radius of 40 km and upper layer thickness of 500–1000 meters, the trend in the curve found by Barth would lead to a reduction in the growth rate of about 60% compared to the flat bottom case, accompanied by a two-fold increase in *e*-folding time. The emerging scenario from all these works, is that the bottom-slope cannot be neglected when the Gulf Stream's path is close to the continental slope, which is the case south of, and in the vicinity of, Cape Hatteras.

In the not-so-typical typical range of $r \leq 2$, the results of the present study can possibly be applied to observed meanders of the Gulf Stream between 75 and 70W. Our estimates of the observable parameters given in Table 2 do not agree with most observations, but Kontoyiannis and Watts (1994) report on observed meanders with wavelengths and phase speeds of 180–212 km and 41–51 km/day, respectively, that agree with the predicted dispersion relationships for radii of deformation ranging between 35 and 45 km (cf Fig. 7). Similarly, Tracey and Watts (1986) find meanders with wavelengths and phase speeds of 120–230 km and 45–46 km/day, respectively, near Cape Hatteras that fit to predicted unstable waves of our theory for depth-ratios ranging between 1 and 2. There is, however, a slight discrepancy between the predicted and calculated growth rates: the *e*-folding time
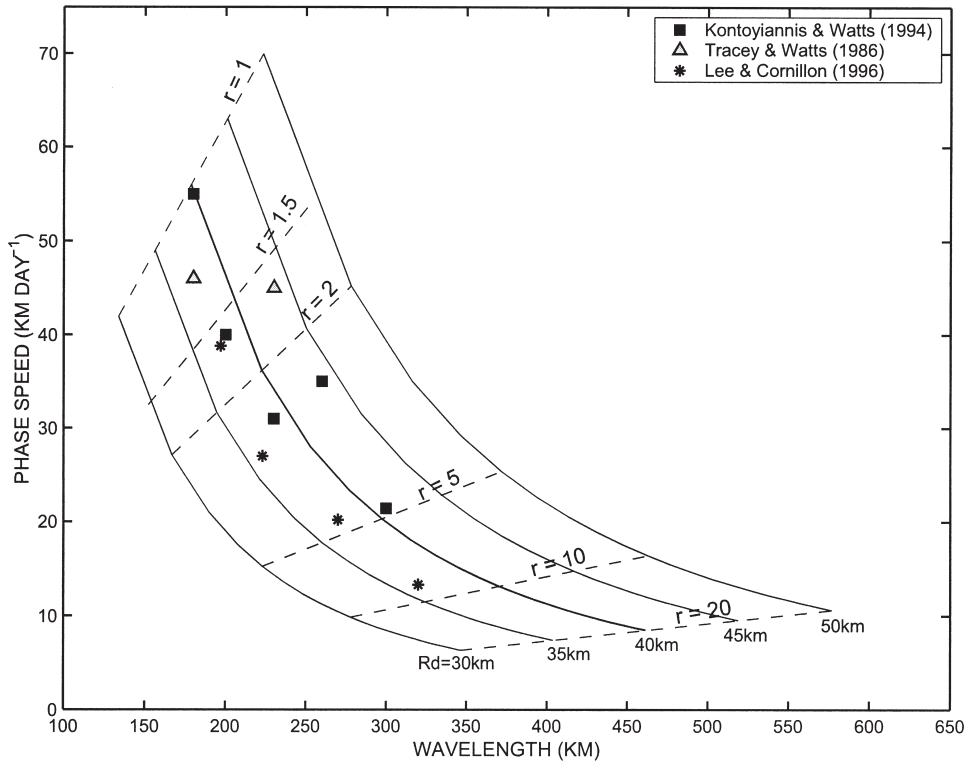
Figure 7. Predicted phase-speed as a function of the wavelength for different radii of deformation, superposed to observations of the Gulf Stream near Cape Hatteras, and between 74 and 70W.

for $1 < r < 2$ is of the order of 0.5 to 1 day, while those reported by Kontoyiannis and Watts (1994) are of the order of 3.5–12 days, and those reported by Tracey and Watts (1986) are 7–8 days. Yet, these observed values remain in a comparable range, especially when taking into account the difficulty in measuring meander growth rates in the real ocean, and the fact that linear instability theories predict only the early stages of meander development: the measured e-folding time of ocean meanders corresponds to a much later stage of development, when its value is expected to change in time. However, the wavelength and phase speed remain fairly close to our theoretical estimates. Another application of our results is in the observations of Lee and Cornillon (1996) who measured Gulf Stream meanders with a 197 km-wavelength and a phase speed of 39 km/day between 74 and 70W. These observed values agree with meander characteristics predicted by our theory for a depth ratio of 1.5. Observations regarding the meanders' growth rate are not reported in their observations. The reason for such similarities in the low depth-ratio range $1 \le r \le 2$ may be due to the proximity of the Gulf Stream to the continental Shelf and Slope in the vicinity of Cape Hatteras, where lateral oscillations of the jet may push its path more inshore, resulting in a relatively shallower subthermocline layer, which in turn, could

trigger the types of instabilities investigated here. In this connection we note that the inclusion of both a sloping bottom and bottom friction will probably yield slower growth rates but the effect of a sloping bottom is to increase the wavelength. Despite these shortcomings of the present theory, there is little doubt that observations in this region are typified by $r < 2$, which is studied in the present work for the first time.

5. Summary

We have studied, semi-analytically, the linear instability of a geostrophic surface front with constant potential vorticity near a wall in a 2-layer shallow water model on an *f*-plane. The dispersion relations we obtained are qualitatively similar to the results of Barth (1989b), yet more accurate for the same depth ratio, and to the results of Killworth *et al.* (1984) when neglecting the influence of the vertical boundary located more than 2 radii of deformation away from the front. We have extended their numerical instability calculations to a wider depth ratio range by including the $1.001 \leq r \leq 20$ subrange. Calculations of the growth rates for r in the vicinity of 1^+ resulted in more precise general fitting functions for several observed parameters as a function of r. These new calculations have also identified a secondary maxima in the growth-rate curves that originates from localized (in wavenumber) resonances between different real modes.

For instance, the general behavior of c_r and c_i is affected by the emergence of another instability source due to the resonance of another mode for $1.005 \leq r < 1.05$, and a secondary lobe (for $\sigma_i(k)$) arises for $k \approx 1.05$.

Most importantly: the growth rates in our calculations are not singular in the $r = 1$ limit, as is the case in quasi-geostrophic analytical solutions for the no wall case (Killworth *et al.,* 1984). Consequently, we found for σ_i, c_r, k_{max} and k_c linear-log dependence in r instead of $r - 1$. Such a difference in the depth ratio range $[1, 2]$ is probably due to the fact that the QG approximation is no longer valid for very thin lower layers. These newly found fitting functions are very close to those suggested by Killworth *et al.* (1984) for $r > 2$.

The limited influence of the wall located at a distance L from the front was explained by deriving an analytical expression for the solution near the wall. These exact solutions provide the boundary conditions at the front for the solutions in the lower layer at the seaward side of the front, so the dependence of the growth rates on L appears only in the weak dependence of the boundary terms $(\coth (kl) + 1)^{-1}$ (for $l = L/R_d$), which varies from 0.43 at $kl = 1$ to 0.5 at $kl = \infty$.

Applications of our results to observations in the Gulf Stream downstream of Cape Hatteras (internal radius of deformation of 40 km, depth ratios ranging from 2 to 10) yield very reasonable agreement with the short wavelength/rapidly growing meanders observed by Watts and Johns (1982), Tracey and Watts (1986), and Kontoyiannis and Watts (1994), which were previously identified in the literature as resulting from predominantly baroclinic instabilities. Comparatively, the fastest growing meanders predicted by this study range in wavelengths, periods, and *e*-folding times respectively, between about (200 km, 8 days, 1.5 days), to about (400 km, 30 days, 4.5 days).

In the vicinity of Cape Hatteras where the proximity of the continental shelf leads to a relatively shallower lower layer of the Gulf Stream, our small r results are applicable. The observed wavelengths and phase speeds of 180–212 km and 39–51 km/day, respectively, from Kontoyiannis and Watts (1994), Tracey and Watts (1986) and Lee and Cornillon (1996) agree with our calculated dispersion relationships in the $1^+ < r < 2$ range for radii of deformation of 35–45 km. Our calculated growth-rate (i.e. e-folding time of the meanders) is slightly larger than the observed one, but this parameter is very difficult to estimate directly from observations in a fast moving current.

REFERENCES

Barth, J. A. 1989a. Stability of a coastal upwelling front. 1. Model development and a stability theorem. J. Geophys. Res., *94,* 10,844–10,856.

—— 1989b. Stability of a coastal upwelling front. 2. Model results and comparison with observations. J. Geophys. Res., *94,* 10,857–10,883.

Boss, E., N. Paldor and L. Thompson. 1996. Stability of a potential vorticity front: from quasigeostrophy to shallow water. J. Fluid Mech., *315,* 65–84.

Boss, E. and L. Thompson. 1999. Mean flow evolution of a baroclinically unstable potential vorticity front. J. Phys. Oceanogr., *29,* 273–287.

Brooks, D. A. and J. M. Bane. 1981. Gulf Stream fluctuations and meanders over the Onslow Bay upper continental slope. J. Phys. Oceanogr., *11,* 247–256.

Chia, F., R. W. Griffiths and P. F. Linden. 1982. Laboratory experiments on fronts. Part II: The formation of cyclonic eddies at upwelling fronts. Geophys. Astrophys. Fluid Dyn., *19,* 189–206.

Cronin, M. 1996. Eddy-mean flow interaction in the Gulf Stream at 68°W. Part II: Eddy forcing on the time-mean flow. J. Phys. Oceanogr., *26,* 2132–2151.

Cronin, M. and D. R. Watts. 1996. Eddy-mean flow interaction in the Gulf Stream at 68°W. Part I: Eddy energetics. J. Phys. Oceanogr., *26,* 2107–2131.

Feliks, Y. and M. Ghil. 1996. Mixed barotropic-baroclinic eddies growing on an eastward midlatitude jet. Geophys. Astrophys. Fluid Dyn., *82,* 137–171.

Griffiths, R. W., P. D. Killworth and M. E. Stern. 1982. Ageostrophic instability of ocean currents. J. Fluid Mech., *117,* 343–377.

Griffiths, R. W. and P. F. Linden. 1982. Laboratory experiments on fronts. Part I: Density-driven boundary currents. Geophys. Astrophys. Fluid Dyn., *19,* 159–187.

Halliwell, G. R. and C. N. K. Mooers. 1983. Meanders of the Gulf Stream downstream of Cape Hatteras 1975–1978. J. Phys. Oceanogr., *13,* 1275–1292.

Hayashi, Y. Y. and W. R. Young. 1987. Stable and unstable shear modes of rotating parallel flows in shallow water. J. Fluid Mech., *184,* 477–504.

Johns, W. E. 1988. One-dimensional baroclinically unstable waves on the Gulf Stream potential vorticity gradient near Cape Hatteras. Dyn. Atm. Oceans, *11,* 323–350.

Killworth, P. D. 1983. Long-wave instability of an isolated front. Geophys. Astrophys. Fluid Dyn., *4,* 235–258.

Killworth, P. D., N. Paldor and M. E. Stern. 1984. Wave propagation and growth on a surface front in a two-layer geostrophic current. J. Mar. Res., *42,* 761–785.

Killworth, P. D. and M. E. Stern. 1982. Instabilities on density driven boundary currents and fronts. Geophys. Astrophys. Fluid Dyn., *23,* 1–28.

Kontoyiannis, H. 1997. Quasi-geostrophic modeling of mixed instabilities in the Gulf Stream near 73 degrees W. Dyn. Atmos. Oceans, *26,* 133–158.

Kontoyiannis, H. and D. R. Watts. 1994. Observations on the variability of the Gulf Stream path between 74°W and 70°W. J. Phys. Oceanogr., *24,* 1999–2013.

Lee, S. K. and G. T. Csanady. 1994. Instability waves in the Gulf Stream front and its thermocline layer. J. Mar. Res., *52,* 837–863.

Lee, T. and P. Cornillon. 1996. Propagation of Gulf Stream meanders between 74° and 70°W. J. Phys. Oceanogr., *26,* 205–224.

Oey, L. Y. 1988. A model of Gulf Stream frontal instabilities, meanders and eddies along the continental slope. J. Phys. Oceanogr., *18,* 211–229.

Orlanski, I. 1968. Instability of frontal waves. J. Atmos. Sci., *25,* 178–200.

—— 1969. The influence of bottom-topography on the stability of jets in a baroclinic fluid. J. Atmos. Sci., *26,* 1216–1232.

Paldor, N. 1983. Linear stability and stable modes of geostrophic fronts. Geophys. Astrophys. Fluid Dyn., *24,* 299–326.

Paldor, N. and M. Ghil. 1991. Shortwave instabilities of coastal currents. Geophys. Astrophys. Fluid Dyn., *58,* 225–241.

—— 1997. Linear instability of a zonal jet on an *f*-plane. J. Phys. Oceanogr., *27,* 2361–2369.

Pedlosky, J. 1987. Geophysical Fluid Dynamics, Springer-Verlag, NY, 710 pp.

Phillips, N. A. 1954. Energy transformation and meridional circulations associated with simple baroclinic waves in a two-level quasi-geostrophic model. Tellus, *6,* 273–286.

Tracey, K. L. and D. R. Watts. 1986. On Gulf Stream meander characteristics near Cape Hatteras. J. Geophys. Res., *91,* 7587–7602.

Watts, D. R. and W. E. Johns. 1982. Gulf Stream meanders: Observations on propagation and growth. J. Geophys. Res., *87,* 9467–9476.

Xue, H. J. and G. Mellor. 1993. Instability of the Gulf Stream front in the South-Atlantic Bight. J. Phys. Oceanogr., *23,* 2326–2350.